Joule

CellPress
OPEN ACCESS

Article

The critical role of the donor polymer in the stability of high-performance non-fullerene acceptor organic solar cells

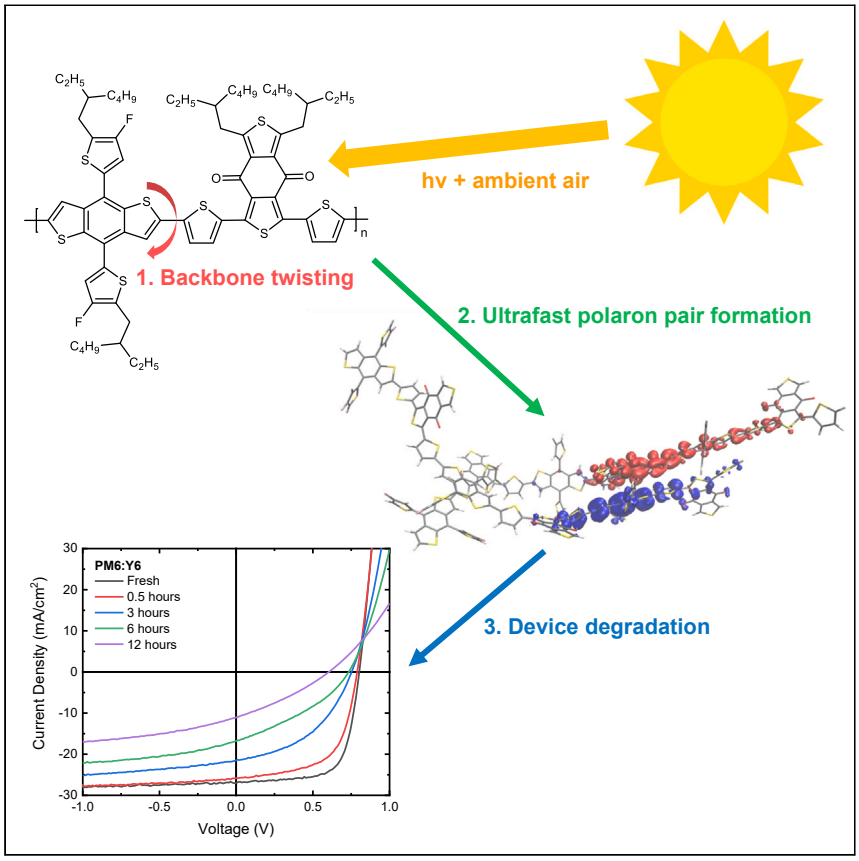

Organic solar cells (OSCs) show great promise for clean energy generation. However, the long-term stability of OSC devices is not good enough for commercial applications. In our work, we identify a light-induced twisting in the backbone of the electron donor polymer, which is enhanced in ambient air, as a dominant degradation mechanism. Thus, we conclude that the donor polymer is an important source of instability in OSCs that must be addressed collectively with the electron acceptor component.

Yiwen Wang, Joel Luke, Alberto Privitera, ..., David Beljonne, Zhe Li, Alexander J. Gillett

zhe.li@qmul.ac.uk (Z.L.)
ajg216@cam.ac.uk (A.J.G.)

Highlights

The degradation mechanisms of 3 representative donor polymers are investigated

Twisting in the polymer backbone is identified as a key degradation mechanism

Backbone twisting is induced by light and enhanced in the presence of ambient air

The donor polymer is identified as the weak link in organic solar cell stability

Wang et al., Joule 7, 810–829
April 19, 2023
https://doi.org/10.1016/j.joule.2023.03.002

CellPress
OPEN ACCESS

Joule

Article

The critical role of the donor polymer in the stability of high-performance non-fullerene acceptor organic solar cells

Yiwen Wang,[1] Joel Luke,[2] Alberto Privitera,[3] Nicolas Rolland,[4] Chiara Labanti,[2] Giacomo Londi,[5] Vincent Lemaur,[4] Daniel T.W. Toolan,[6] Alexander J. Sneyd,[7] Soyeong Jeong,[8] Deping Qian,[8] Yoann Olivier,[5] Lorenzo Sorace,[3] Ji-Seon Kim,[2] David Beljonne,[4] Zhe Li,[1,*] and Alexander J. Gillett[7,9,*]

SUMMARY

The poor operational stability of non-fullerene electron acceptor (NFA) organic solar cells (OSCs) currently limits their commercial application. While previous studies have primarily focused on the degradation of the NFA component, we also consider here the electron donor material. We examine the stability of three representative donor polymers, PM6, D18, and PTQ10, paired with the benchmark NFA, Y6. After light soaking PM6 and D18 in air, we find an enhanced conversion of singlet excitons into trapped interchain polaron pairs on sub-100 femtosecond timescales. This process outcompetes electron transfer to Y6, significantly reducing the charge generation yield. However, this pathway is absent in PTQ10. We identify twisting in the benzo[1,2-*b*:4,5-*b*′]dithiophene (BDT)-thiophene motif shared by PM6 and D18 as the cause. By contrast, PTQ10 does not contain this structural motif and has improved stability. Thus, we show that the donor polymer can be a weak link for OSC stability, which must be addressed collectively with the NFA.

CONTEXT & SCALE

Organic solar cells (OSCs) show great promise for clean energy generation. Recent progress in non-fullerene electron acceptor (NFA) material design has improved the power conversion efficiencies (PCEs) of OSCs to nearly 20%. This level of performance is now suitable for real-world deployment. However, such applications also require long-term stability from the photovoltaic modules. This has not yet been achieved in the best-performing devices that use derivatives of the NFA Y6. In this work, we examine the degradation mechanisms of OSCs fabricated from the benchmark NFA Y6 and three representative electron donor polymers, PM6, D18, and PTQ10. We identify a light-induced twisting in a shared structural motif of PM6 and D18 as a dominant degradation mechanism, which is enhanced in the presence of ambient air. By contrast, PTQ10 does not contain this structural motif and shows improved stability. Thus, the donor polymer is an important source of instability that must be addressed in OSCs.

INTRODUCTION

Through the development of non-fullerene electron acceptors (NFAs), the power conversion efficiencies (PCEs) of organic solar cells (OSCs) have rapidly increased, now exceeding 19%.[1,2] However, while the performance of OSC devices is approaching the levels required for their mainstream deployment, such applications also require long-term stability from the photovoltaic modules. Some NFA OSC blends have demonstrated excellent stability, with extrapolated T_{80} lifetimes (time taken for the solar cell PCE to drop to 80% of its initial value) of over 20 years,[3,4] but this has not yet been simultaneously achieved in systems that currently give the best PCEs in NFA OSCs to date.[5] Therefore, successful commercialization necessitates that substantial effort be dedicated to understanding and engineering out the causes of instability in high-performance NFA OSC systems, such as those based on Y6 and their derivatives.[5,6] When considering the degradation mechanisms of an OSC device, it is important to note that performance losses may result from a complex combination of factors.[7–9] This can include not only an innate instability in the materials or morphology of the polymer:NFA bulk heterojunction (BHJ)[10–12] but also chemical degradation of the blend induced by interlayers in the device stack,[13–15] or degradation of the device stack itself.[16] Although the latter two issues can be remedied through careful device engineering, including appropriate selection of the interlayers and encapsulation materials,[3,4,17–19] any intrinsic instability

in the blend components presents a more fundamental challenge that must be addressed separately.

We report here on the intrinsic degradation mechanisms in the BHJ layers of efficient NFA OSCs under light soaking. We begin by focusing on the benchmark PM6:Y6 system (chemical structures in Figure 1A),[6] as many OSCs comprise a "Y-series" NFA paired with the PM6 donor polymer.[2,5,20,21] Subsequently, we expand our study to include two other high-performance donor polymers, D18[22] and PTQ10[23] (chemical structures in Figure 4A). While Y6 shows excellent photostability, the polymers PM6 and D18 both exhibit the same severe degradation mechanism, involving the ultrafast conversion of singlet excitons (S_1) into trapped polaron pair (PP) states. We identify a shared structural motif in PM6 and D18 that is responsible for this behavior. By contrast, PTQ10 does not contain this motif and hence shows an improved intrinsic photostability. Thus, while the field is heavily focused on advancing the design of NFAs, we propose that the donor polymer design is equally important and should not be overlooked when considering strategies to improve the stability of high-performance NFA OSCs.

RESULTS AND DISCUSSION

Fresh and light-soaked PM6:Y6 solar cell characteristics

We begin by investigating the degradation mechanisms intrinsic to the benchmark PM6:Y6 blend. Here, we have fabricated inverted devices with the structure of ITO (indium tin oxide)/ZnO/PM6:Y6/MoO_3/Ag. To ensure that degradation is limited to—as far as possible—the PM6:Y6 active layer, we have deposited the PM6:Y6 film on top of the ITO/ZnO layers, before light soaking the samples under 1-sun equivalent white LED illumination with no UV spectral component. Following light soaking, fresh layers of MoO_3 and Ag are evaporated on top of the BHJ layer to complete the device. Previous studies have indicated that the ZnO layer can play a significant role in the degradation of the donor and acceptor components in OSC devices, including Y6,[24] as the surface hydroxyl groups can cause the UV-induced photocatalytic degradation of the carbon–carbon double bonds.[25] To minimize the influence of this extrinsic factor on the intrinsic material degradation pathways we seek to investigate here, we have used an LED light source with no UV component for aging and performed control measurements for BHJ films on glass and conventional devices using PEDOT:PSS (poly(3,4-ethylenedioxythiophene) polystyrene sulfonate), which both show a similar level of degradation to the ZnO samples (Figures S1 and S2; Table S1). Therefore, we rule out a significant contribution from ZnO to the sample degradation for the relatively short light-soaking timescales investigated here. For the degradation protocol, we focus on PM6:Y6 films light soaked in ambient air as they show the largest change in their optical properties (*vide infra*). We note that the extremely high-quality encapsulation required for the long-term exclusion of ambient air from an OSC comprises a significant cost of the photovoltaic module.[26] Furthermore, the roll-to-roll processing required to make OSC modules on a large scale is generally performed in ambient air, allowing for the incorporation of oxygen and water into the BHJ film.[27] Thus, we consider exploring the degradation processes in air to be highly relevant to OSCs,[9,28,29] where high-throughput fabrication and lower-cost (and therefore less isolating) encapsulation materials are required for commercially competitive photovoltaic modules. We shall return to the important point of photodegradation in an inert nitrogen atmosphere versus ambient air later in the manuscript.

In Figure 1B, we present the current density-voltage (J-V) characteristics of the fresh PM6:Y6 devices and devices where the BHJ was selectively light soaked for 0.5, 3, 6,

[1]School of Engineering and Materials Science, Queen Mary University of London, Mile End Road, London E1 4NS, UK

[2]Department of Physics and Centre for Processable Electronics, Imperial College London, South Kensington SW7 2AZ, UK

[3]Department of Chemistry "Ugo Schiff" and INSTM RU, University of Florence, Via della Lastruccia 3-13, 50019 Sesto Fiorentino, Firenze, Italy

[4]Laboratory for Chemistry of Novel Materials, Université de Mons, Place du Parc 20, Mons, Belgium

[5]Laboratory for Computational Modelling of Functional Materials, Namur Institute of Structured Matter, Université de Namur, Rue de Bruxelles, 61, 5000 Namur, Belgium

[6]Department of Chemistry, University of Sheffield, Dainton Building, Brook Hill, Sheffield S3 7HF, UK

[7]Cavendish Laboratory, University of Cambridge, JJ Thomson Avenue, Cambridge CB3 0HE, UK

[8]Department of Chemistry and Centre for Processable Electronics, Imperial College London, 82 Wood Lane, London W12 7TA, UK

[9]Lead contact

*Correspondence: zhe.li@qmul.ac.uk (Z.L.), ajg216@cam.ac.uk (A.J.G.)

https://doi.org/10.1016/j.joule.2023.03.002

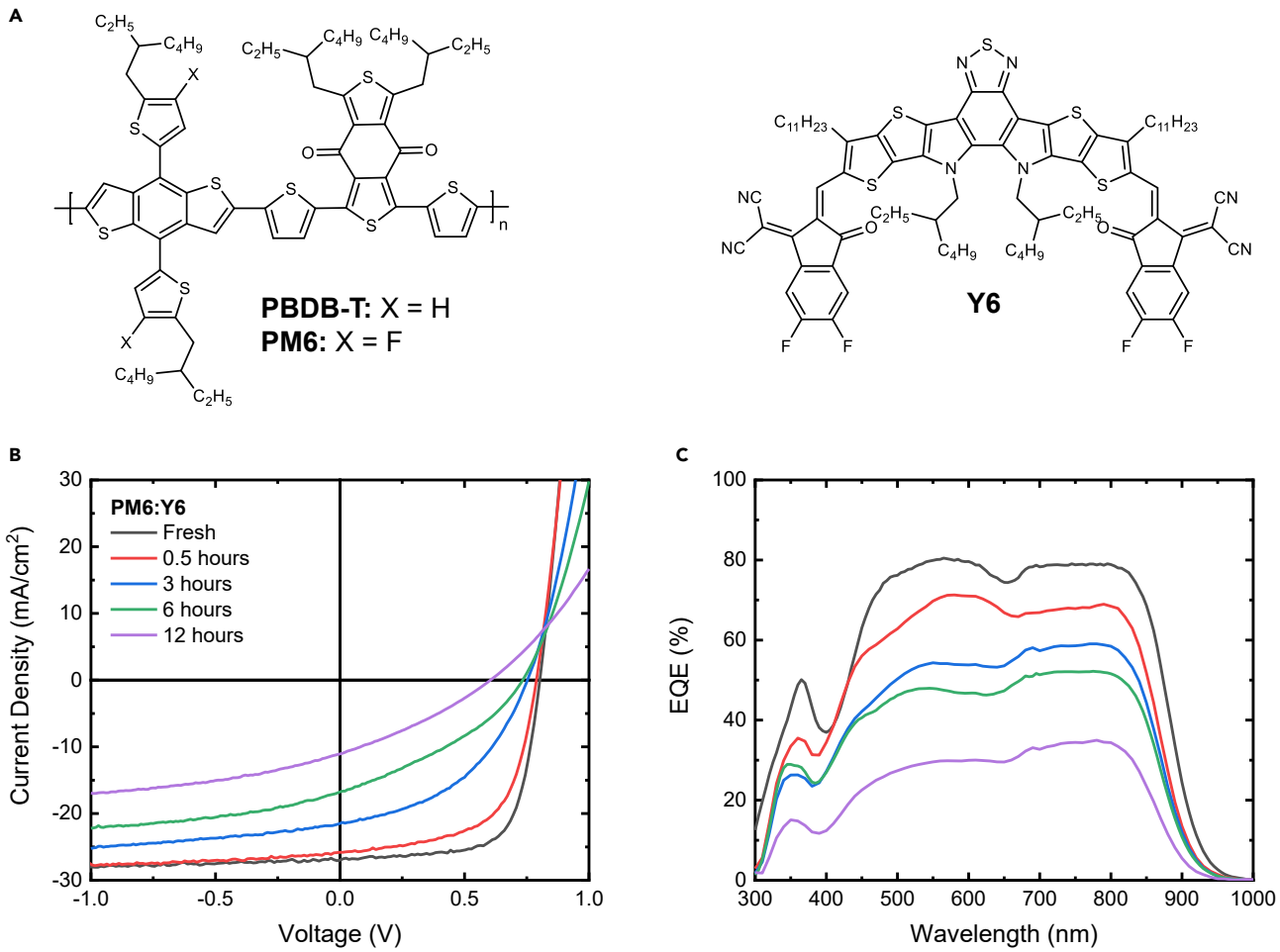

Figure 1. Chemical structures and solar cell performance

(A) The chemical structures of the donor polymers, PBDB-T and PM6, and the acceptor material Y6, explored in this study.

(B) The current density-voltage curves of the PM6:Y6 solar cells where the BHJ layer was light soaked for varying timescales under 1-sun intensity white LED illumination in ambient air. Device measurements were performed under 100 mW/cm^2 AM1.5G solar illumination.

(C) The corresponding external quantum efficiency (EQE) curves of the aged PM6:Y6 solar cells presented in (B).

and 12 h (photovoltaic parameters are summarized in Table 1). Fresh devices show a PCE of 14.9%, with a short-circuit current density (J_{SC}) of 26.99 mA/cm^2, an open-circuit voltage (V_{OC}) of 0.80 V, and a fill factor (FF) of 68.8%. Upon light soaking, the device performance decreases severely, indicating significant degradation of the PM6:Y6 BHJ. To decouple the effect of light soaking from light-induced sample heating, we have annealed the partial (ITO/ZnO/PM6:Y6) device stack at 85°C in the dark for 12 h before evaporating on the top contacts (Figure S3). Here, we find no noticeable change in performance between the annealed and fresh device and thus conclude that thermal effects contribute negligibly to the observed degradation behavior for the aging timescales in our study. The external quantum efficiency (EQE) spectrum of the fresh and aged blends is substantially reduced across the whole spectrum after light soaking (Figure 1C), possibly due to the increased trap-induced recombination in the aged blends (*vide infra*). This will reduce the charge extraction efficiency and cause the EQE to drop equally across the whole spectrum. However, the region between 500 and 700 nm that corresponds to the PM6 absorption shows a stronger decrease (Figure S5), suggesting that charge generation

Table 1. The device performance parameters of the fresh and aged PM6:Y6 solar cell devices

Light soaking time	PCE (%)	V_{OC} (V)	J_{SC} (mA/cm^2)	FF (%)
Fresh	14.87	0.80	26.99	68.77
0.5 h	12.38	0.79	25.81	60.89
3 h	7.30	0.75	21.50	45.04
6 h	4.27	0.73	16.75	34.73
12 h	2.05	0.60	11.08	30.65

pathways from excitons created on PM6 are more affected than those from Y6. Further studies on the light intensity dependence of the device parameters reveal an increase in the trap-mediated recombination in the PM6:Y6 BHJ following light soaking (Figure S6; Table S4). Light-induced electron paramagnetic resonance (L-EPR) and transient absorption (TA) studies corroborate the increased trap-mediated recombination and further reveal that PM6, and not Y6, is responsible (Figures S7, S8, and S20). This is attributed to PM6 becoming more defective with a higher density of deep traps after light soaking. A full discussion of the light intensity dependence of the device parameters and the L-EPR results is presented in the supplemental information.

Steady-state optical characterization of PM6 and Y6

To understand the degradation mechanisms taking place in the PM6:Y6 active layer, we begin by characterizing the films using steady-state techniques. In Figure 2A, we show the UV-vis absorption spectrum of fresh and aged neat PM6 and Y6 films, with the corresponding neat and blend films aged in ambient air and nitrogen displayed in supplemental information (Figures S10 and S11). To demonstrate most clearly the impact of light soaking, we focus herein on films light soaked in air for 12 h where the greatest degree of degradation is expected to occur but return to the samples light soaked in nitrogen later. We observe no significant change in the absorption spectrum of the neat Y6 film (Figure 2A) after light soaking, and the photoluminescence (PL) quantum efficiency (PLQE) effectively remains constant within the experimental error of $\pm$0.1%: 2.0% in the fresh and 2.1% in the aged film (Y6 emission spectra shown in Figure S12). However, the absorption spectrum of PM6 clearly changes after light soaking in air for 12 h. While there is only a small decrease in the absorption magnitude of the PM6 band centered at 600 nm upon aging, the vibronic structure of this feature is lost in the neat film (Figure 2A) and PM6:Y6 blend (Figure S11A). We also note an increased intensity in the PM6 absorption tail, potentially indicating a larger number of sub-band-gap states. Importantly, there is no significant change in the PM6 (or Y6) film absorption spectrum after 12 h of annealing in the dark at 85°C, further indicating that the degradation is solely due to processes arising after photon absorption by the polymer and not from light-induced heating of the film (Figure S13). In addition to the absorption changes, we find that the PLQE drops from 0.3% in the fresh PM6 film to below the detection limit of our experimental setup (<0.1%) in the aged film (emission spectra shown in Figure 4D), signifying an enhancement of the non-radiative processes quenching bright S_1 states in PM6.

To probe the PM6 absorption changes further, we have performed highly sensitive photothermal deflection spectroscopy (PDS) absorption measurements on fresh and aged neat PM6 films, as well as fresh and aged PM6:Y6 blend films (Figure 2B). PDS reveals a more prominent absorption tail and a significant increase in the Urbach energy of neat PM6 after light soaking to 84.8 meV, compared with 49.3 meV in the fresh film. This observation, along with the loss of the vibronic peak progression in the PM6 absorption spectrum (well-resolved vibronic features are associated with

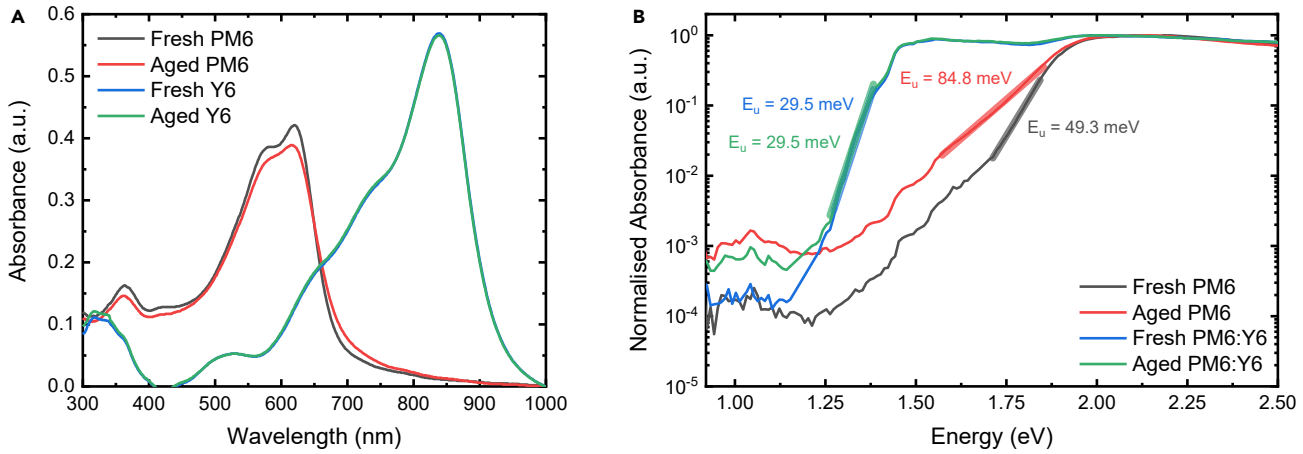

Figure 2. The steady-state absorption spectra of fresh and aged PM6 and Y6 films

(A) The UV-vis absorption spectra of neat PM6 and Y6 films. Absorption spectra for both fresh films and samples light soaked for 12 h in ambient air are shown.

(B) The absorption spectra of PM6 and the PM6:Y6 blend films measured with photothermal deflection spectroscopy. Spectra for both fresh films and samples light soaked for 12 h in ambient air are shown. The Urbach energy, obtained from fitting the absorption tail of the samples (fit indicated by the thick semitransparent line), is also included on the plot.

a higher degree of ordering between the polymer chains[30]), confirms that light soaking increases the energetic disorder and density of sub-gap states in the PM6 domains.[31,32] By contrast, the PDS absorption of the fresh and aged PM6:Y6 blends has an identical Urbach energy for the Y6 absorption tail of 29.5 meV. We also observe an increase in the intensity of the sub-band-gap absorption feature around 1 eV in both the light-soaked neat PM6 and PM6:Y6 blend films. As this band is present in the neat PM6 film, we determine that it represents an increased density of PM6 trap states,[31–33] in line with the OSC device and L-EPR studies. We therefore conclude that the primary changes in the blend upon light soaking occur in the PM6 domains. This is supported by grazing incidence wide-angle X-ray scattering (GIWAXS) studies, which show a decrease in the molecular ordering in neat PM6 upon light soaking (Figure S14; see supplemental information for full discussion).

Transient absorption studies of PM6 and Y6

To better understand how the sample degradation is linked to the loss in photovoltaic performance, we have studied the fresh and aged PM6, Y6, and blend films, using TA spectroscopy. As with the steady-state measurements, we find no significant difference between the photophysics of fresh and aged neat Y6 films (Figure S15). In the corresponding PM6:Y6 blends, with selective excitation of Y6 at 800 nm (Figure S16), we observed no change in the intrinsic hole transfer rate but a slower quenching of the excited states generated on Y6 in the aged blend. As a result, there is a small reduction in the charge yield of the aged PM6:Y6 blend following excitation of Y6. These observations are consistent with the donor:acceptor (D:A) de-mixing previously observed in PM6:Y-series NFA blends,[11] which increases the average distance that photogenerated excitons must diffuse to the D:A interface. This will lead to a larger fraction of excitations on Y6 recombining prior to hole transfer, although potentially to no change to the intrinsic rate of hole transfer, as this is instead primarily governed by the morphology at the interface and not by the donor and acceptor domain sizes.

As our previous results suggest that PM6 is more affected by light soaking than Y6, we primarily focused on the photophysics of the donor polymer. We begin with the

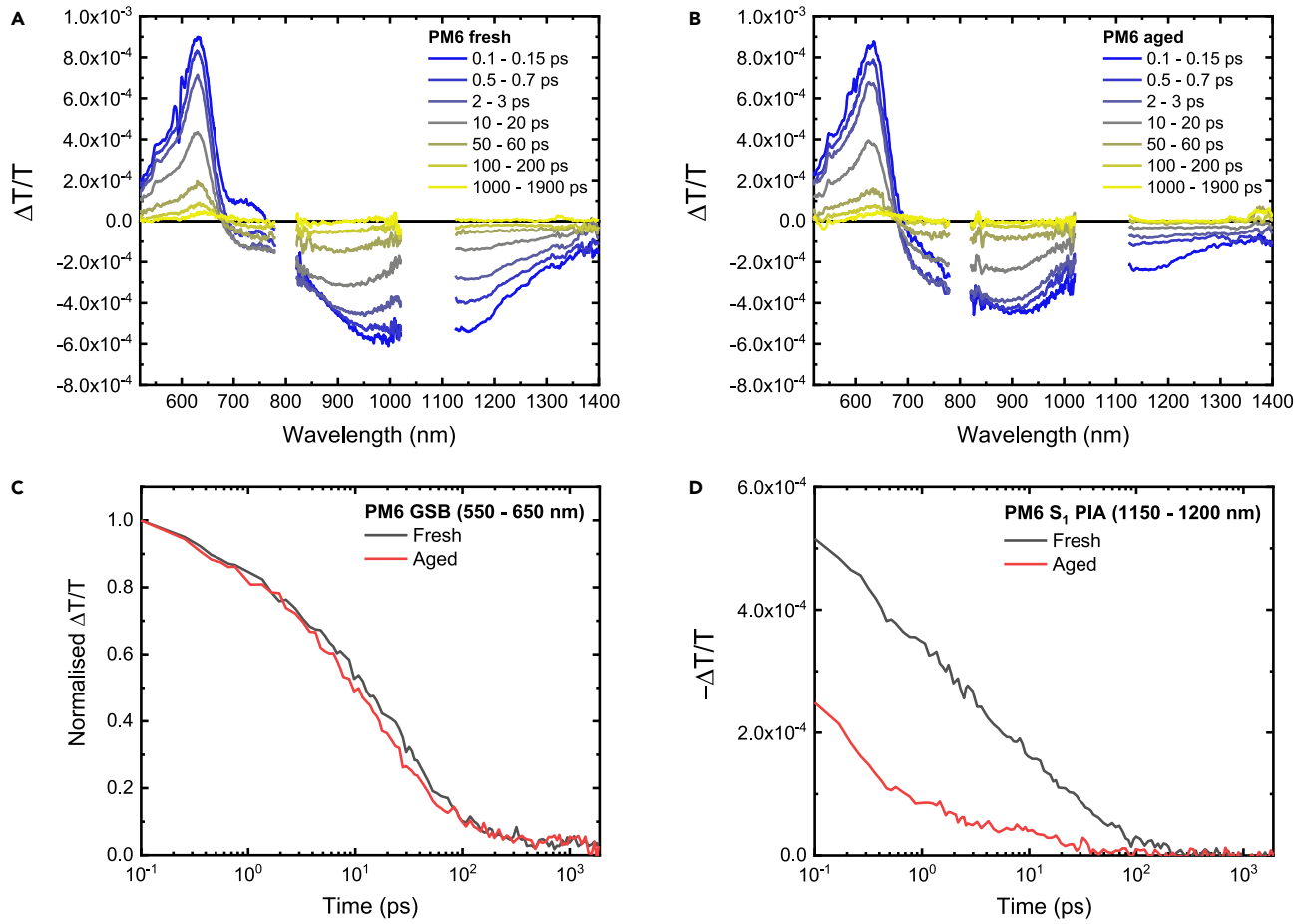

Figure 3. The transient absorption spectra and kinetics of fresh and aged PM6 films

(A) The TA spectra of the fresh neat PM6 film, excited at 580 nm with a fluence of 0.64 μJ/cm^2.

(B) The TA spectra of the neat PM6 film, light soaked for 12 h in ambient air, excited at 580 nm with a fluence of 0.64 μJ/cm^2.

(C) The normalized kinetics of the PM6 GSB region (550–650 nm), taken from the fresh and aged neat PM6 films.

(D) The raw kinetics of the PM6 S_1 PIA (1,150–1,200 nm), taken from the fresh and aged PM6 films.

TA of the fresh PM6 film (Figure 3A). After excitation at 580 nm, we observed the PM6 ground-state bleach (GSB) between 550–650 nm, a weak PM6 stimulated emission (SE) band at 720 nm, and a broad photo-induced absorption (PIA) extending into the near infrared, with a peak at 1,150 nm. The SE band and PIA at 1,150 nm provide clear fingerprints for the presence of PM6 S_1 states. Interestingly, we observed the decay of the PM6 SE and S_1 PIA on picosecond (ps) timescales, accompanied by the formation of a new band at 920 nm. Through comparison to the TA of a reference PM6:$PC_{60}BM$ blend (Figure S17), we assign this feature to the PM6 hole polaron. We therefore conclude that in the fresh PM6 film, S_1 states convert to interchain PPs[34]; this has been observed in polymer films where close contact between the individual chains allows for interchain charge transfer (CT) to take place.[35–38] However, given the short PM6 GSB lifetime (Figure 3C) and low PLQE of the fresh PM6 film (0.3%), we conclude that the PP states formed are tightly bound and do not achieve long-range charge separation, resulting in rapid non-radiative recombination.

We next turn to the TA of the aged PM6 film (Figure 3B), also excited at 580 nm. Despite the similar absolute absorbance of the fresh and aged PM6 films at the

excitation wavelength of 580 nm (Figure 2A), the intensity of the PM6 S_1 PIA at 1,150 nm is a factor of two lower in the aged film at 0.1–0.15 ps after excitation with the same fluence (Figure 3D). The resolvable decay kinetic of the S_1 PIA after 0.1 ps also shows a more rapid decrease in the aged film. In addition, the PM6 SE band is almost completely quenched by 0.1–0.15 ps, while the hole polaron PIA at 920 nm is nearly fully formed at this time. Thus, we conclude that the rate of interchain PP formation in PM6 is significantly increased upon light soaking in air, with a substantial fraction of the PPs formed on sub-100 femtosecond (fs) timescales; this is consistent with the unmeasurable PLQE (<0.1%) of the aged PM6 film, as nearly all the PM6 S_1 states are quenched by PP formation before they can emit. Interestingly, we note that the PM6 hole polaron PIA in aged PM6 appears to have a similar intensity to fresh PM6. To explain this, we consider that the extremely low PLQE of 0.3% in fresh PM6 suggests that the fraction of S_1 states forming PPs is already very high, possibly approaching unity. Thus, even if the PPs form faster in the aged blend, the absolute yield cannot increase much and the polaron PIA intensities are expected to be comparable. To account for the faster rate of PP formation in aged PM6, we note that an increased Urbach energy is related to a larger number of sub-gap states and trap sites.[31–33] Therefore, we propose that the greatly increased Urbach energy of the aged PM6 film (Figure 2B) reflects a higher density of sub-gap states in PM6 domains, meaning that PM6 S_1 states have a greater chance of being generated near a site favorable for the formation of bound PP states.[39] Furthermore, we find very similar changes in the absorption spectrum (Figure S23) and TA (Figure S24) of the parent compound, PBDB-T (chemical structure in Figure 1A). Thus, we confirm that the increased disorder and enhanced PP formation upon light soaking appear to be intrinsic to this family of polymers.

In the TA of the fresh and aged PM6:Y6 blend films with preferential excitation of PM6 at 580 nm (Figure S18), we find that the interchain PP formation is fast enough to out-compete electron transfer to Y6 (see supplemental information for detailed discussion). Furthermore, as the interchain PPs in PM6 have a much shorter lifetime and slower transport through the PM6 domains than S_1 states,[34] they are susceptible to recombining before reaching the D:A interface for electron transfer to Y6. Indeed, we observed a divergence in the PM6 GSB kinetics of the fresh and aged blend films on the same tens of ps timescales that the interchain PP states recombine over (Figure S18C). Therefore, as the PM6 S_1 states are more rapidly funneled through this channel in the aged samples, this results in increased losses through interchain PP recombination. The impact of the PP loss channel is clearly seen in the nanosecond (ns) TA measurements of the fresh and aged blend films. Here, the intensity of the PM6 hole polaron signal in the aged blend film is about half that of the fresh blend after charge transfer has been completed at 1 ns (Figure S19). This difference in the hole polaron yield also agrees well with the roughly factor of two lower intensity of the PM6 S_1 PIA at 100 fs in the aged PM6 and PM6:Y6 blend film TA (Figures 3D and S18D), indicating that the free charge carrier yield following the electron transfer process is severely limited by the PM6 interchain PP loss pathway.

Investigation of other donor polymer classes

Although donor polymers from the PBDB-T family, including PM6, are among those most frequently paired with Y-series acceptor materials in high-performance OSCs, other donor polymers have also demonstrated excellent performance with this class of NFAs. Two prominent examples are D18[22] and PTQ10[23] (chemical structures in Figure 4A). D18 shares some structural similarities with PM6, as both comprise a benzo[1,2-*b*:4,5-*b*′]dithiophene (BDT) donor unit, with bridging thiophenes between the donor and acceptor moieties. By contrast, PTQ10 is a thiophene-quinoxaline

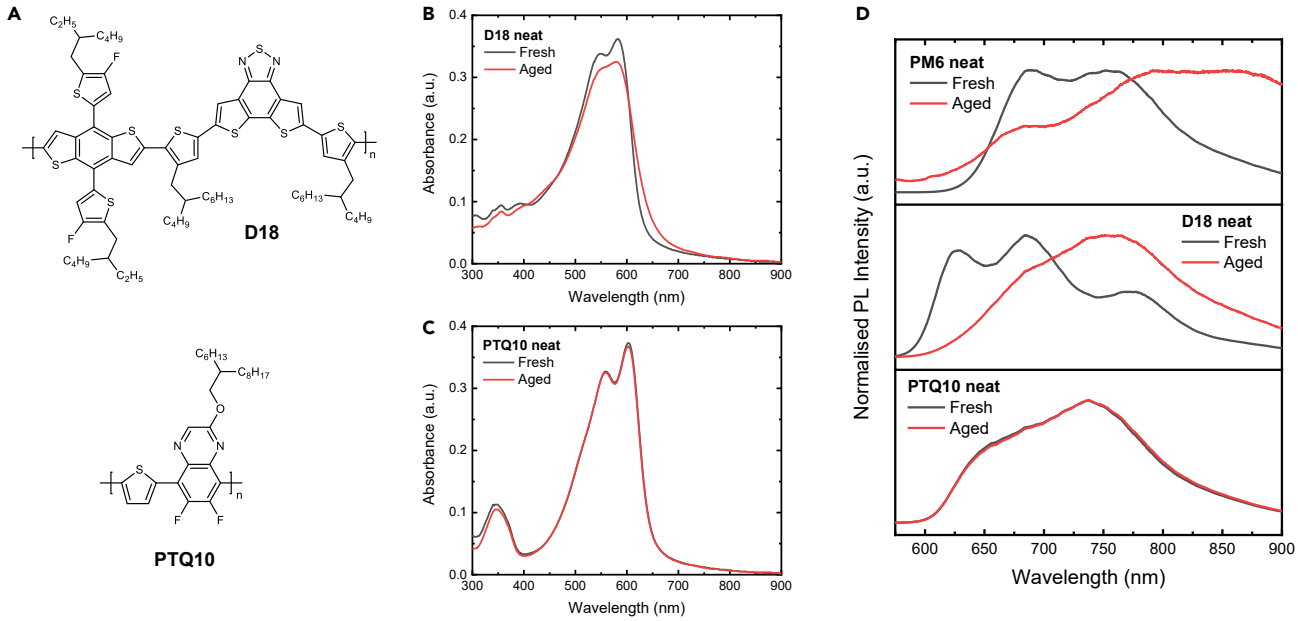

Figure 4. The steady-state absorption and photoluminescence spectra of fresh and aged D18 and PTQ10 films

(A) The chemical structures of D18 and PTQ10.

(B) The UV-vis absorption spectra of neat D18. Absorption spectra for both a fresh film and a sample light soaked for 12 h in ambient air are shown.

(C) The UV-vis absorption spectra of neat PTQ10. Absorption spectra for both a fresh film and a sample light soaked for 12 h in ambient air are shown.

(D) The normalized photoluminescence spectra of fresh and aged PM6, D18, and PTQ10 films.

co-polymer that is structurally distinct from both PM6 and D18. Inverted D18:Y6 and PTQ10:Y6 OSC devices, with the same device stack and aging protocol as the PM6:Y6 devices (12 h light soaking the ITO/ZnO/BHJ layers in air under white LED illumination), show a smaller loss in performance than PM6:Y6 (Figures S25 and S26; Tables S6 and S7). However, the PTQ10:Y6 devices exhibit the smallest decrease in performance upon light soaking for both inverted and conventional architectures, potentially indicating an improved stability of this donor polymer compared with PM6 and D18. Again, we confirm that ZnO does not make a significant contribution to the aging processes of these polymers on the timescales of our study through comparison of ZnO samples to control films on glass and conventional architecture devices with PEDOT:PSS (Figures S25–S28).

To better understand the degradation mechanisms in D18 and PTQ10, we have fully characterized both polymers and their blends with Y6, using steady-state absorption, TA, and PL spectroscopies. A full account of the results is presented in the supplemental information, but we focus here on the key points for brevity. In the steady-state absorption spectra, we observed qualitatively the same degradation behavior after 12 h of light soaking for D18 as for PM6, with a loss in the vibronic progression in the main absorption band around 580 nm and a significant increase in the intensity of the absorption tail (Figure 4B). However, PTQ10 appears to be remarkably stable, with almost no change in the absorption spectrum after light soaking (Figure 4C). These changes in the neat polymer films upon light soaking are also mirrored in the blend films with Y6, where we observe considerable degradation in the polymer absorption in D18:Y6 and negligible change in PTQ10:Y6 (Figures S27C and S28C). The findings in the steady-state absorption spectra are reflected in the TA, where we observe an enhanced formation of interchain PPs in aged D18 (Figures S30 and S31), with little difference between the fresh and aged PTQ10

films (Figure S35). Consistent with the results for PM6, the PP formation also has a significant impact on the electron transfer process in aged D18:Y6 (Figure S32), while we also find evidence for D:A phase separation that impacts the hole transfer process (Figure S33D). By contrast, there is virtually no change between fresh and aged PTQ10:Y6 (Figures S36 and S37). As a result, we conclude that PTQ10 is intrinsically a much more photostable donor polymer than PM6, PBDB-T, or D18, and it forms a more thermodynamically stable BHJ with Y6.

The presence of significant PP formation in PM6 and D18, but not in PTQ10, is further supported by PL studies. Consistent with the PLQE measurements, the emission of the neat PM6 polymer is significantly quenched following light soaking (93%). Similar PL quenching behavior is observed in D18 (90%), while the quenching of PTQ10 emission is only 53% (Figure S38A). The reduction of PM6 and D18 emission is also accompanied by a change in spectral shape, with the high energy emission being selectively quenched, whereas PTQ10 demonstrates no change in emission shape with aging (Figure 4D). To unravel the nature of the emissive species in the polymers, the PL lifetime was measured using time-correlated single-photon counting (TCSPC; Figure S38B). We find that the emission peaks of fresh PM6 and D18 films correlate to different emissive species with distinct PL lifetimes, while fresh PTQ10 shows the same lifetime across the emission spectra. The multiple emissive species in PM6 and D18, with a longer lifetime observed for longer wavelength emission, are consistent with the presence of sub-band-gap interchain PP states, even in the fresh films; PPs are expected to have a lower energy, as well as a smaller oscillator strength and thus slower emission than S_1 states. Conversely, PTQ10 shows only S_1 formation and emission, indicating a more energetically homogeneous energy and morphological landscape. This can be linked to the characteristic molecular structure of PTQ10, where a more rigid and planar bond is present between quinoxaline and thiophene units. By contrast, the BDT-thiophene (BDT-T) linkage in PM6 and D18 is more flexible (see simulation results in Figure S39). Interestingly, the three polymers that show similar photodegradation behavior with increased interchain PP losses upon light soaking—PM6, PBDB-T, and D18—all share the same BDT-T structural motif. By contrast, the more photostable PTQ10 has a different thiophene-quinoxaline backbone. This raises the question as to whether there is an intrinsic instability to light soaking in air for the BDT-T motif.

Identifying the cause of degradation with Raman spectroscopy

To investigate the light-induced changes at a molecular level, we utilized Raman spectroscopy, which has been previously used to track molecular structure and conformational changes during the light soaking of organic semiconductors.[12,40] As shown in Figure 5A, after 12 h of light soaking, there is a slight change in spectral shape of the PM6 and D18 Raman spectra. Specifically, a small reduction in the intensity of the peak associated with both the BDT and flanking thiophene units at ~1,470 cm^{-1}, as deduced from the simulated PM6 Raman spectrum (Figure S40; Table S8; the displacement vectors of the calculated mode at 1,466 cm^{-1} are shown in Figure S41). To confirm and exaggerate this small change, the films were light soaked in air for 60 h; the absorption spectra for PM6 and D18 exhibit similar but more extreme changes than the 12-h aged samples, while the absorption of PTQ10 shows a comparatively small change (Figure S42). The normalized Raman spectra before and after the 60-h aging are shown in Figure 5B, indicating a clear relative quenching of the ~1,470 cm^{-1} peak in both PM6 and D18 upon light soaking. Additionally, all the lower frequency (1,400–1,525 cm^{-1}) peaks of PM6 are quenched relative to the peak at 1,540 cm^{-1}. For PTQ10 there is a small relative quenching of the 1,575 cm^{-1} peak, but the changes are much less pronounced

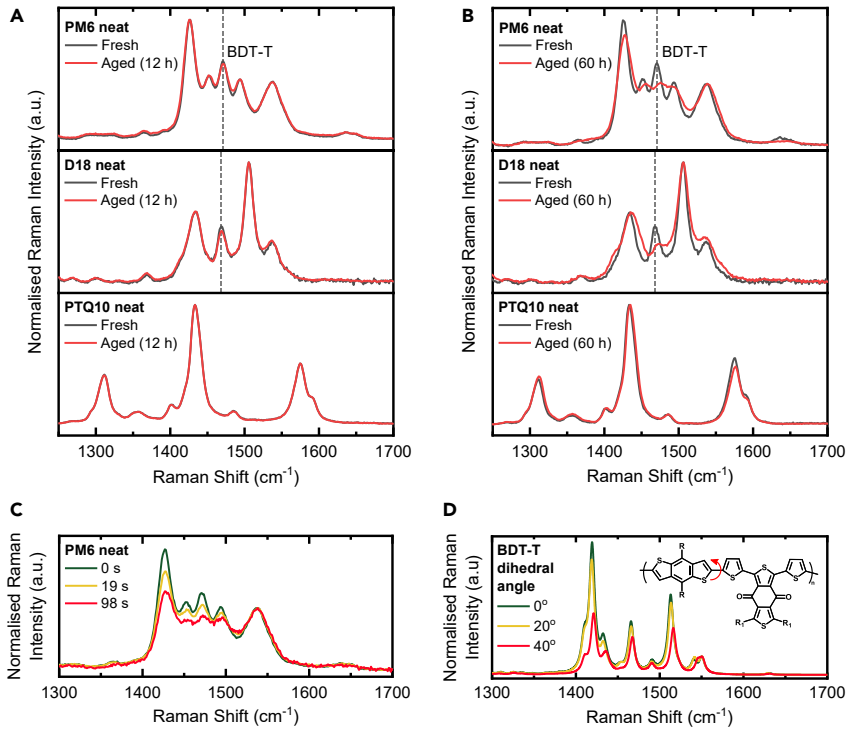

Figure 5. Raman measurements of fresh and aged polymer films

(A) Normalized Raman spectra taken at 514 nm excitation for fresh and aged polymer films, with films aged by light soaking in ambient air for 12 h. The spectra are normalized to the ~1,540 cm^{-1} peak for PM6, the ~1,500 cm^{-1} peak for D18, and the ~1,430 cm^{-1} peak for PTQ10. The ~1,470 cm^{-1} peak associated with the BDT-T linkage in PM6 and D18 is marked with the dashed line.

(B) Normalized Raman spectra taken at 514 nm excitation of fresh and aged polymer films, with films aged by light soaking in ambient air for 60 h to enhance the spectral changes. The spectra are normalized to the same peaks as the 12-h aged samples. The ~1,470 cm^{-1} peak associated with the BDT-T linkage in PM6 and D18 is marked with the dashed line.

(C) Normalized (to the ~1,540 cm^{-1} peak) Raman spectra of a PM6 film as a function of degradation time, taken at 514 nm excitation. The film was degraded *in situ* by the 514 nm laser in air.

(D) Normalized (to the ~1,540 cm^{-1} peak) simulated Raman spectra of a monomer of PM6 as a function of the inter-unit dihedral angle between the BDT and thiophene units, highlighted in the chemical structure.

than the other two polymers, consistent with its superior photostability. These results clearly demonstrate that the BDT-T motif in the PM6 and D18 polymers is affected by light soaking in air.

To follow the degradation further, we have conducted *in situ* 514 nm laser degradation for a neat PM6 film, which allows us to rapidly follow and exaggerate peak changes under strong light intensity. Figure 5C shows the normalized spectra as a function of laser degradation time; the peak changes are consistent with those observed after 60 h, although the lower-frequency peaks are further quenched. This behavior is also seen for the PM6 features in the PM6:Y6 blend, confirming that the same degradation mechanism is operating in both (Figure S43). Density functional theory (DFT) simulations were carried out to determine the origin of this spectral evolution. Firstly, we find no good correlation between the evolution of the PM6 Raman spectrum and several potential oxidation products (Figure S44). Along with the lack of any obvious new C–O or C=O bonds in the Fourier transform

infrared (FTIR) spectra of PM6 (or indeed either of the other polymers) after light soaking in air (Figure S45), we rule out a significant amount of direct oxidation of the polymers. The absence of oxidation is also supported by air photoemission spectroscopy (APS; Figure S46), where the onset of photoemission (essentially the highest occupied molecular orbital [HOMO] levels of the polymers) is unchanged. The simulated Raman spectra of a PM6 monomer as a function of BDT-T dihedral angle is given in Figure 5D. In resemblance to the experimental spectra, there is a clear quenching of the lower-frequency modes relative to the peak at 1,540 cm^{-1}, suggesting that we may be observing a conformational distortion away from planarity in the BDT-T linkage of the polymer backbone. The specific role of this motif in the degradation process is confirmed by simulated Raman spectra as a function of the dihedral angles between other backbone units (Figure S47), where only BDT-T twisting (Figure 5D) matches the experimental results.

Finally, it is worth considering the role of environmental molecules, such as oxygen and water, in the degradation process. As noted above, the photodegradation of PM6 appears to be accelerated in the presence of ambient air. This is consistent with a previous report that proposed a then-undefined degradation process in PM6:Y6 devices specifically involving the combined exposure to light and air.[41] However, our FTIR measurements rule out significant oxidation of the polymer backbone after light soaking in air for 12 h (Figure S45). Therefore, in line with the findings on photodegradation in some NFAs, we propose that oxygen or water is interacting non-covalently with the conjugated backbone.[12] This can affect the potential energy surface for bond rotation in conjugated polymers by changing the dielectric surroundings, allowing for new energetic minima conformations to be adopted.[42] We suggest that this behavior could be related to the reversible interaction between environmental oxygen molecules and the sulphur atoms in PM6 that has been shown to occur.[43] As light is required for this conformational change to take place, this indicates that the non-covalent interactions are happening specifically with the excited species of the polymer. However, earlier work has also indicated that PM6 is the weak link in PM6:Y6 OSCs over longer device light-soaking timescales (hundreds of hours) in a nitrogen environment.[44] Therefore, it is possible that while oxygen or water speeds up the backbone twisting process we observe, similar effects may still eventually occur in their absence. This points to the general weakness of the donor polymer in NFA OSCs, especially in materials employing the BDT-T motif.

Computational studies of the PM6 morphology

To understand the nature of the interchain PP states experimentally observed, we have combined classical force field molecular dynamics (MD) simulations and quantum-chemical time-dependent DFT (TDDFT) excited-state calculations to probe the morphology dependence of sites amenable to PP formation. Our MD simulations of the PM6 bulk material show an overall amorphous structure. The relative flexibility of the polymer chains combined with the steric interactions induced by the side chains leads to a high degree of structural disorder with multiple polymer chain conformations, preventing any long-range ordering in the bulk. Yet, the radial distribution function (RDF) calculated for every donor and acceptor moiety in the bulk reveals a non-negligible density of interchain close contacts (Figure 6A). While these contacts exist for [acceptor]-[acceptor], [donor]-[donor], and [donor]-[acceptor] pairs, they are tighter for interchain [donor]-[acceptor] pairs, with a minimum distance down to ~3.5 Å. The spatial distribution functions (SDFs) of the [donor]-[acceptor] pairs also reveal a preferential co-facial orientation (Figure S49). By contrast, the [donor]-[donor] contacts start above 3.7 Å and become particularly pronounced from 4 Å on, due to the steric interactions between the fluorinated thiophenes flanking the donor moieties.

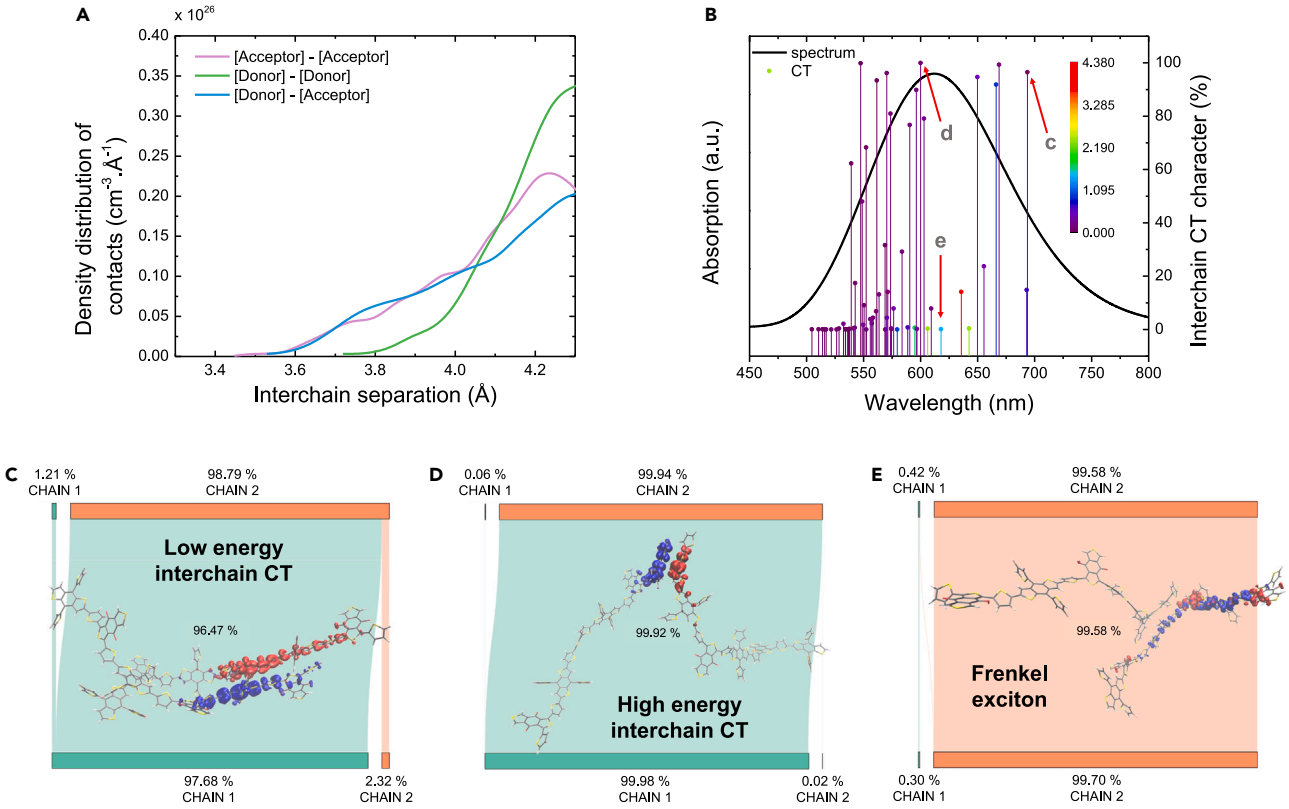

Figure 6. Theoretical calculations of PM6 excited states and interchain contacts

(A) Radial distribution functions for pairs of donor/acceptor moieties.

(B) The average optical absorption spectrum and interchain CT character of selected excited states, colored by their corresponding oscillator strength (red = high, purple = low) for close [donor]-[acceptor] contacts.

(C–E) Hole and electron densities, in blue and red, respectively, for selected interchain CT excited states as indicated in (B). The transition diagrams show the distribution of the hole (bottom) and electron (top) on the two polymers (CHAIN 1, CHAIN 2). The interchain CT character is determined as the percentage of charge transferred from one chain to the other (i.e., 96.47% in C, 99.92% in D, and 0.12% in E).

Thus, our MD simulations show that the topology of the PM6 chains is amenable to close [donor]-[acceptor] interchain contacts. To check whether these contacts could sustain low-lying interchain CT excitations, equivalent to PPs, we have simulated the optical properties of the films. From the MD trajectories, we have selected polymer (2-chain) aggregates with close [donor]-[acceptor] contacts and performed excited-state calculations using an optimally tuned screened range-separated hybrid (RSH) DFT functional,[45,46] see experimental procedures. Figure 6B shows the calculated optical absorption spectrum obtained by averaging over all the investigated configurations. The simulated spectrum shows a broad absorption peaking around 620 nm (2.00 eV) with an extended low-energy tail, in good agreement with the experimental results. To assess the nature of the excited states, we have calculated the hole and electron densities and associated transition diagrams, from which we have derived their degree of interchain CT character. A selection of the most relevant excitations, colored by their corresponding oscillator strengths (purple = low, red = high), are superimposed on the absorption spectrum in Figure 6C (all excitations are shown in Figure S50). The plot reveals a large density of predominantly interchain CT states that carry relatively low oscillator strengths across the whole excitonic density of states (EDoSs). These interchain CT excitations correspond to very different forms of aggregates existing in the bulk PM6, as shown in

Figures 6C and 6D. The diversity of the contacts makes it difficult to draw clear correlations between polymer conformations and the nature of the interchain CT states. Nevertheless, it seems that very local contact points tend to promote higher-energy interchain CT states (Figure 6D), whereas more extended contacts give rise to lower-energy CT states (Figure 6C). Most importantly, our TDDFT calculations suggest the exclusive existence of weakly emissive interchain CT excitations (or PPs) at the bottom of the EDoS. By contrast, Frenkel excitations confined over single polymer chains are located at higher energies only (Figure 6E).

To understand how the light and ambient air induced twisting around the BDT-T linkage could be driving the enhanced interchain PP formation in PM6 films, we have examined the planarity of the PM6 chains in our MD simulations. Here, we have defined a planarity factor (PF) for the PM6 backbone, which captures how the bonds of the BDT-T motif distort away from planarity (see supplemental information for details of the PF). By analyzing the PF for all the PM6 chains in our MD simulations, we find a clear link between less planar BDT-T units and closer [donor]-[acceptor] contacts, defined here as [donor]-[acceptor] interaction distances <4.5 Å (Figure S53). This indicates that the formation of close [donor]-[acceptor] contacts involves some steric interactions that require the BDT-T linkages to move away from planarity. We therefore propose that the presence of more twisted polymer chains around the BDT-T linkage, as induced by light soaking in air, can promote the development of the close [donor]-[acceptor] contacts required for the formation of interchain PPs. This then results in the creation of more sites in PM6 domains that can sustain low-energy PPs, which in turn increases the likelihood of PM6 S_1 states being photogenerated near such a location. Thus, the speed at which PM6 S_1 states are converted into interchain PPs would be expected to increase following light soaking in air, in line with experimental observations.

Conclusions

In our work, we have investigated the degradation pathways intrinsic to high-performance NFA OSCs based on Y6. Promisingly, we find that Y6 demonstrates excellent photostability. However, while the donor polymer PTQ10 also shows good photostability, PM6 and D18 show rapid and qualitatively similar degradation processes. We attribute this to a light-induced dihedral twisting around the BDT-T motif shared by both PM6 and D18, which is enhanced in the presence of ambient air. This process results in the increased formation of detrimental interchain PP states on sub-100 fs timescales and higher levels of trap-mediated recombination in the devices. Thus, we conclude that a key factor limiting the stability of high-performance OSCs utilizing Y-series NFAs is the donor polymer. To address this, we propose that the field should seek to design novel polymer donors free from the problematic BDT-T structural motif and with an improved planarity and rigidity in the backbone. This can be achieved by conformational locking using non-covalent interactions or sterically hindered linkages. Hence, we consider PTQ10 as representing a promising starting point for further development. However, the encouraging photostability of Y6 indicates that if more stable donor polymers can be identified and developed, NFA OSCs have the potential to simultaneously demonstrate the high-performance and long operational lifetimes necessary for widespread commercial utilization.

EXPERIMENTAL PROCEDURES

Resource availability

Lead contact

Further information and requests for resources and materials should be directed to and will be fulfilled by the lead contact, Alexander J. Gillett (ajg216@cam.ac.uk).

Materials availability

This study did not generate new unique materials.

Data and code availability

The data that support the plots within this paper is available at the University of Cambridge Repository (https://doi.org/10.17863/CAM.95682).

Organic solar cell device fabrication

PM6 and Y6 were purchased from Solarmer, while PTQ10 and D18 were purchased from 1 Material. Neat PM6, PTQ10, D18, and Y6 solutions were prepared in chloroform at 8, 6, 4, and 10 mg mL^{-1}, respectively. PM6:Y6 (1:1.2) and PTQ10:Y6 (1:1.2) blends were dissolved in chloroform with 0.5% chloronaphthalene (CN), while the D18:Y6 (1:1.2) blend was dissolved in chloroform alone. All organic solutions were stirred at 40°C for at least 4 h before use. The substrates were cleaned by ultrasonication sequentially with acetone, dilute detergent solution, deionized water, acetone, and isopropanol for 20 min each before being dried under a stream of nitrogen and treated with UV-ozone immediately prior to use. For the inverted devices, ZnO sol-gel was then spin-coated on the ITO substrates and annealed at 150°C for 10 min in air. After transferring samples to the glovebox with O_2 and H_2O levels <0.1 ppm, the active layer (80–100 nm) was spin-coated on the ZnO/ITO surface. The samples were then light soaked for varying timescales (0.5, 3, 6, and 12 h) under 1-sun intensity white LED illumination in ambient air or nitrogen. Then, the samples were transferred to the adjacent vacuum chamber with a base pressure of $<2.0 \times 10^{-6}$ Pa for deposition of a 10 nm thick MoO_3 interlayer and a 100 nm thick Ag top electrode. For the conventional devices, PEDOT:PSS was spin-coated on the ITO substrates and annealed at 140°C for 10 min in air. The active layer (80–100 nm) was then spin-coated on top of the PEDOT:PSS, followed by light-soaking for 12 h under 1-sun intensity white LED illumination in ambient air or nitrogen, where applicable. Then, samples were transferred to the evaporation chamber for the deposition of Ca (20 nm) and Al (100 nm). The OSCs have an identical active area of 0.045 cm^2, defined by the overlap area of the anode and the cathode. The active area of the device was determined using an optical microscope.

Organic solar cell device testing

J-V characteristics of fresh and aged OSC devices were measured under AM1.5G illumination of 100 mW/cm^2 using a xenon lamp solar simulator in an inert environment. Eight individual solar cell devices were tested for each aging timescale reported. A Keithley 2635A source measurement unit was used to scan the voltage applied to the solar cell between −2 to 1 V at a speed of 0.43 V/s with a dwell time of 46 ms. Light intensity of the solar simulator was calibrated using a single crystalline silicon detector (with a KG-5 filter) to minimize the spectral mismatch. A Bentham PVE300 photovoltaic QE system was used to obtain the EQE spectrum over the wavelength range 300–1,000 nm. The standardized data reporting for photovoltaic cells is provided in Data S1.

Transient absorption spectroscopy

TA was performed on a setup powered using a commercially available Ti:sapphire amplifier (Spectra Physics Solstice Ace). The amplifier operates at 1 kHz and generates 100 fs pulses centered at 800 nm with an output of 7 W. An optical parametric amplifier (OPA; Light Conversion TOPAS) was used to provide the tuneable ~100 fs pump pulses for the ps TA measurements. For the ns TA measurements, the second harmonic (532 nm) of an electronically triggered, Q-switched Nd:YVO_4 laser (Innolas Picolo 25) provided the ~1 ns pump pulse. The probe pulses were provided by broadband non-collinear OPAs (NOPAs) operating in the visible and near infrared

spectral regions. The probe pulses are collected with an InGaAs dual-line array detector (Hamamatsu G11608-512DA), driven and read out by a custom-built board from Stresing Entwicklungsbüro. The probe beam was split into two identical beams by a 50/50 beamsplitter. This allowed for the use of a second reference beam which also passes through the sample but does not interact with the pump. The role of the reference was to correct for any shot-to-shot fluctuations in the probe that would otherwise greatly increase the structured noise in our experiments. Through this arrangement, very small signals with a $\frac{\Delta T}{T} = 1 \times 10^{-5}$ could be measured.

Photoluminescence quantum efficiency measurements

The PLQE was determined using method previously described by De Mello et al.[47] Samples were placed in an integrating sphere and photoexcited using a 658 nm continuous-wave laser. The laser and emission signals were measured and quantified using calibrated Andor iDus DU420A BVF Si and Andor CCD-1430 InGaAs detectors.

Light-induced electron paramagnetic resonance spectroscopy

Light-induced EPR measurements were performed at X-band ($\nu \sim 9.40$ GHz) on a Bruker Elexsys E500 spectrometer, equipped with a ^{4}He continuous flow cryostat (ESR 900, Oxford Instruments) for measurements at variable temperatures (10 and 40 K). All the spectra were acquired by using the same modulation frequency (100 kHz), modulation amplitude (1 G), microwave power (0.02 mW, 40 dB) and receiver gain (60 dB). The reported spectra were averaged 49 times. The magnetic field was calibrated with a crystal of 2,2-diphenyl-1-picrylhydrazyl (DPPH). For sample illumination, Thorlabs laser diodes ($\lambda \sim 534$ and 785 nm) were focused in front of the optical access of the EPR spectrometer cavity (Bruker ST102). The system delivered about 35 and 50 mW of light power to the sample at 534 and 785 nm, respectively. The power was measured at the output of the laser diode, before the EPR cavity grid. EPR spectral simulations were carried out using the core functions *pepper* and *esfit* of the open-source MATLAB toolbox EasySpin.[48]

EPR samples were fabricated by spin-coating solutions under identical conditions to the optimized devices onto Mylar substrates, which were subsequently cut into strips with a width of 3 mm. To ensure the flexible Mylar substrates did not bend during the spin coating process, they were mounted onto rigid glass substrates using adhesive tape. Ten strips were placed in quartz EPR tubes; the same amount of material in each sample ensures that EPR intensities can be compared for the equivalent fresh and aged neat or blend film samples excited with the same wavelength. The EPR tubes were sealed in a nitrogen glovebox with a mono-component resin, ensuring that all EPR measurements were performed without oxygen exposure.

Photothermal deflection spectroscopy

PDS sensitively measures absorption directly by probing the heating effect in samples upon absorption of light. Films were coated on a Spectrosil fused silica substrate and were immersed in an inert liquid FC-72 Fluorinert. They were then excited with a modulated monochromated light beam perpendicular to the plane of the sample. A combination of a Light Support MKII 100 W Xenon arc source and a CVI DK240 monochromator was used to produce a modulated monochromated light beam. The PDS measurements were acquired by monitoring the deflection of a fixed wavelength (670 nm) diode laser probe beam following absorption of each monochromatic pump wavelength.

Raman spectroscopy

Raman spectroscopy and PL measurements were taken using a Renishaw inVia Raman microscope in a backscattering configuration with a 50× objective and

holographic notch filters to remove Rayleigh scattered light. A diffraction grating with 2,400 L/mm is used for Raman measurements, while a 300 L/mm grating is used for PL measurements. A 514 nm excitation is used for all measurements with the laser power being adjusted depending on the measurement, *in situ* degradations were carried out with a 514 nm laser with an approximate power density of 26 MW m^{-2}, which results in a degradation acceleration factor of 25,000×, although in practice the laser spot (d = 10 μm) is defocused during degradation so this factor will be significantly reduced. For steady-state measurements, samples were placed in a Linkam stage under a constant nitrogen flow. *In situ* degradation measurements were carried out in air with no nitrogen flow.

For simulating the experimental Raman spectra, single-molecule gas-phase simulations based on DFT were performed using Gaussian 09 software on the Imperial College High Performance Computing service, with GaussView 6 utilized for result visualization. DFT was applied at the B3LYP level with 6-311G(d,p) basis set. The calculations are carried out on monomers end-capped with thiophenes, and alkyl side chains are approximated as methyl groups. All molecular structures were optimized to the energy minimum, while dihedral scans were performed by freezing the desired dihedral coordinate and relaxing the rest on the molecule to optimized geometry. For simulation of Raman vibrational modes, the empirical wavenumber scaling factor of 0.97 was applied for consistency with experimental data.

Fourier transform infrared spectroscopy

Attenuated total reflection Fourier transform infrared (ATR-FTIR) spectroscopy measurements were performed using Agilent Cary 630 spectrometer with a diamond ATR accessory. The sample substrate was Al foil as this can enhance the signal intensity.[49] A new background spectrum was collected prior to the analysis of a new sample. Al foil was placed onto glass slides and fixed with tape to facilitate ease of handling and archiving. PM6, D18, and PTQ10 solutions were deposited in the same way as described above in the device fabrication section. Aged films were light-soaked under white LED illumination ambient air for 12 h before the measurement.

Air photoemission spectroscopy

APS measurements were taken using an APS04 Air Photoemission System (KP Technology) using a 2 mm gold tip under atmospheric conditions. All samples were grounded via the bottom contact, ITO. The cube root of photoemission is plotted to determine the onset of photoemission in accordance with the protocol described by Baikie et al.[50]

Grazing incidence wide-angle X-ray scattering

Grazing incidence wide-angle X-ray scattering (GIWAXS) was performed on the Xuess instrument equipped with an Excillum MetalJet liquid gallium X-ray source. Alignment was performed on silicon substrates via three iterative height (z) and rocking curve (Ω) scans, with the final grazing incidence angle set to $\Omega = 0.2^{\circ}$. Scattering patterns were recorded on a vertically offset Pilatus 1M detector with a sample to detector distance of 327 mm, calibrated using a silver behenate standard to achieve a q range of 0.045–1.85 $Å^{-1}$. Two-dimensional images were recorded with exposure times of 900 s. The images were masked to remove the sample horizon, detector module gaps and beamstop. Data correction and reduction were performed using the GIXSGUI MATLAB toolbox.[51]

Time-correlated single photon counting

Time-correlated single photon counting Photoluminescence (PL) and time-correlated single photon counting (TCSPC) measurements were taken using an Edinburgh

Instruments FLS1000 spectrometer with the sample in a reflection configuration with the excitation source and detector perpendicular to each other. A monochromated xenon lamp (405 nm) was used as the excitation for PL measurements and a 405 nm picosecond pulsed diode laser was used for time-correlated measurments. The lifetimes at different emission wavelengths were measured and an instrument response function (IRF) was obtained using a clean quartz substrate.

Computational modeling

The ground-state geometry optimizations of an isolated PM6 trimer and the Y6 NFA were performed at the DFT level, using the ωB97X-D functional and the 6-31G(d,p) basis set. All the alkyl chains were replaced by methyl groups to speed up the DFT optimizations, carried out with the Gaussian 16 software.[52] Then, magnetic properties of the charged species (i.e., the PM6 cation and the Y6 anion) were computed at the B3LYP/Def2-TZVP level of theory. Namely, g-tensor calculations were performed by using gauge including atomic orbitals (GIAOs[53]) and the RIJCOSX approximation. These calculations were done using the ORCA 4.2 code.[54]

To calculate the structural properties of the bulk PM6 material, we simulated the supramolecular organization of an amorphous PM6 phase by MD with the LAMMPS package[55] using a tailored force field derived from DREIDING[56] and following the protocol detailed in the supplemental information. The radial distribution functions (RDFs were calculated considering the centers of mass of the donor and acceptor units, as defined in Figure S48, and accumulated over multiple frames during the MD production run. The spatial distribution functions (SDFs around each unit were built from the same frames using the VIAMD software.[57–59] From the RDF we selected all donor-acceptor local contacts with a distance smaller than 4 Å and performed excited-state calculations on the corresponding dimers, removing the side chains and saturating the bonds for computational efficiency.

Excited-state calculations were performed using time dependent density functional theory (TDDFT) within the Tamm-Dancoff approximation (TDA), and using a range-separated hybrid (RSH LC-ωhPBE functional and the 6-311G(d,p) basis set. The range separation parameter ω was optimally tuned at ω = 0.1050 $Bohr^{-1}$ and *screened* RSH calculations were performed setting α = 0.2000 and β = 0.2212 to mimic the dielectric constant of toluene.[45] These calculations were performed with the Gaussian 16 software.[52] The lowest 20 excited states were considered in the calculations, and further characterized by analyzing the hole and electron wave functions using the Multiwfn software.[60] Transition diagrams were calculated using the Electrans python package.[61]

SUPPLEMENTAL INFORMATION

Supplemental information can be found online at https://doi.org/10.1016/j.joule.2023.03.002.

ACKNOWLEDGMENTS

A.J.G. thanks the Leverhulme Trust for an Early Career Fellowship (ECF-2022-445). Y.W. and Z.L. acknowledge the funding of UK Engineering and Physical Sciences Research Council (EPSRC) (EP/S020748/1 and EP/S020748/2). J.-S.K., J.L., and C.L. also acknowledge the UK EPSRC for the Plastic Electronics Centre for Doctoral Training grant (EP/L016702/1) and the ATIP Program Grant (EP/T028513/1). A.P. acknowledges funding by the Italian Ministry of Education and Research (MIUR) under the National Recovery and Resilience Plan (NRRP), Mission 4 Component 2

Investment 1.2—Call for tender no. 247 of 19/08/2022 (project ID: SOE_0000064, photodriven spin selectivity in chiral organic molecules and devices—PHOTOCODE). L.S. and A.P. acknowledge support from the MIUR through PRIN project 2017 "quantum detection of chiral-induced spin selectivity at the molecular level" (2017Z55KCW) and Progetto Dipartimenti di Eccellenza 2018-2022 (ref. B96C1700020008). Computational resources were provided by the Consortium des Équipements de Calcul Intensif (CÉCI), funded by the Fonds de la Recherche Scientifiques de Belgique (F.R.S. – FNRS) under grant no. 2.5020.11, as well as the Tier-1 supercomputer of the Fédération Wallonie-Bruxelles, infrastructure funded by the Walloon Region under grant agreement no. 1117545. G.L. and Y.O. acknowledge funding by the Fonds de la Recherche Scientifique – FNRS under grant no. F.4534.21 (MIS-IMAGINE). This work has received funding from the European Union's Horizon 2020 research and innovation programme under grant agreement no. 964677. D.B. is a FNRS Research Director. We thank Richard Friend for helpful discussions. We also acknowledge the research group of James Durrant at Imperial College London, in particular Pabitra Shakya Tuladhar.

AUTHOR CONTRIBUTIONS

A.J.G., Y.W., and Z.L. conceived the work. A.J.G. performed the TA and PLQE measurements. Y.W. characterized the OSC devices, prepared the samples for the spectroscopy studies, and performed the steady-state absorption measurements. J.L. and C.L. performed the Raman, APS measurements, and simulated the Raman spectra. A.P. conducted the L-EPR studies. N.R., V.L., and D.B. performed and analyzed the MD and excited-state calculations. G.L. and Y.O. carried out the magnetic property calculations. A.J.S. measured the PDS. D.T.W.T. carried out the GIWAXS measurements. S.J. helped prepare the D18 and PTQ10 films and devices. D.Q. performed the PL measurements. Y.O., L.S., J.-S.K., D.B., and Z.L. supervised their group members involved in the project. A.J.G., Y.W., and Z.L. wrote the manuscript with input from all authors.

DECLARATION OF INTERESTS

The authors declare no competing interests.

Received: January 18, 2022
Revised: November 2, 2022
Accepted: March 10, 2023
Published: April 19, 2023

REFERENCES

1. Zhu, L., Zhang, M., Xu, J., Li, C., Yan, J., Zhou, G., Zhong, W., Hao, T., Song, J., Xue, X., et al. (2022). Single-junction organic solar cells with over 19% efficiency enabled by a refined double-fibril network morphology. Nat. Mater. *21*, 656–663. https://doi.org/10.1038/s41563-022-01244-y.

2. Cui, Y., Xu, Y., Yao, H., Bi, P., Hong, L., Zhang, J., Zu, Y., Zhang, T., Qin, J., Ren, J., et al. (2021). Single-junction organic photovoltaic cell with 19% efficiency. Adv. Mater. *33*, e2102420. https://doi.org/10.1002/adma.202102420.

3. Xu, X., Xiao, J., Zhang, G., Wei, L., Jiao, X., Yip, H.-L., and Cao, Y. (2020). Interface-enhanced organic solar cells with extrapolated T80 lifetimes of over 20 years. Sci. Bull. (Beijing) *65*, 208–216. https://doi.org/10.1016/j.scib.2019.10.019.

4. Li, Y., Huang, X., Ding, K., Sheriff, H.K.M., Ye, L., Liu, H., Li, C.-Z., Ade, H., and Forrest, S.R. (2021). Non-fullerene acceptor organic photovoltaics with intrinsic operational lifetimes over 30 years. Nat. Commun. *12*, 5419. https://doi.org/10.1038/s41467-021-25718-w.

5. Li, S., Li, C., Shi, M., and Chen, H. (2020). New phase for organic solar cell research: emergence of Y-series electron acceptors and their perspectives. ACS Energy Lett. *5*, 1554–1567. https://doi.org/10.1021/acsenergylett.0c00537.

6. Yuan, J., Zhang, Y., Zhou, L., Zhang, G., Yip, H.-L., Lau, T.-K., Lu, X., Zhu, C., Peng, H., Johnson, P.A., et al. (2019). Single-junction organic solar cell with over 15% efficiency using fused-ring acceptor with electron-deficient core. Joule *3*, 1140–1151. https://doi.org/10.1016/j.joule.2019.01.004.

7. Li, W., Liu, D., and Wang, T. (2021). Stability of non-fullerene electron acceptors and their photovoltaic devices. Adv. Funct. Mater. *31*, 2104552. https://doi.org/10.1002/adfm.202104552.

8. Burlingame, Q., Ball, M., and Loo, Y.-L. (2020). It's time to focus on organic solar cell stability. Nat. Energy *5*, 947–949. https://doi.org/10.1038/s41560-020-00732-2.

9. Wang, Y., Lee, J., Hou, X., Labanti, C., Yan, J., Mazzolini, E., Parhar, A., Nelson, J., Kim, J., and

Li, Z. (2021). Recent progress and challenges toward highly stable nonfullerene acceptor-based organic solar cells. Adv. Energy Mater. *11*, 2003002. https://doi.org/10.1002/aenm.202003002.

10. Ghasemi, M., Hu, H., Peng, Z., Rech, J.J., Angunawela, I., Carpenter, J.H., Stuard, S.J., Wadsworth, A., McCulloch, I., You, W., et al. (2019). Delineation of thermodynamic and kinetic factors that control stability in non-fullerene organic solar cells. Joule *3*, 1328–1348. https://doi.org/10.1016/j.joule.2019.03.020.

11. Qin, Y., Balar, N., Peng, Z., Gadisa, A., Angunawela, I., Bagui, A., Kashani, S., Hou, J., and Ade, H. (2021). The performance-stability conundrum of BTP-based organic solar cells. Joule *5*, 2129–2147. https://doi.org/10.1016/j.joule.2021.06.006.

12. Luke, J., Speller, E.M., Wadsworth, A., Wyatt, M.F., Dimitrov, S., Lee, H.K.H., Li, Z., Tsoi, W.C., McCulloch, I., Bagnis, D., et al. (2019). Twist and degrade—impact of Molecular Structure on the photostability of nonfullerene acceptors and their photovoltaic blends. Adv. Energy Mater. *9*, 1803755. https://doi.org/10.1002/aenm.201803755.

13. Hu, L., Liu, Y., Mao, L., Xiong, S., Sun, L., Zhao, N., Qin, F., Jiang, Y., and Zhou, Y. (2018). Chemical reaction between an ITIC electron acceptor and an amine-containing interfacial layer in non-fullerene solar cells. J. Mater. Chem. Mater. *6*, 2273–2278. https://doi.org/10.1039/C7TA10306A.

14. Wang, Y., Lan, W., Li, N., Lan, Z., Li, Z., Jia, J., and Zhu, F. (2019). Stability of nonfullerene organic solar cells: from built-in potential and interfacial passivation perspectives. Adv. Energy Mater. *9*, 1900157. https://doi.org/10.1002/aenm.201900157.

15. Wang, Y., Han, J., Cai, L., Li, N., Li, Z., and Zhu, F. (2020). Efficient and stable operation of nonfullerene organic solar cells: retaining a high built-in potential. J. Mater. Chem. Mater. *8*, 21255–21264. https://doi.org/10.1039/D0TA08018G.

16. Grossiord, N., Kroon, J.M., Andriessen, R., and Blom, P.W.M. (2012). Degradation mechanisms in organic photovoltaic devices. Org. Electron. *13*, 432–456. https://doi.org/10.1016/j.orgel.2011.11.027.

17. Liu, S.-W., Lee, C.-C., Su, W.-C., Yuan, C.-H., Shu, Y.-S., Chang, W.-C., Guo, J.-Y., Chiu, C.-F., Li, Y.-Z., Su, T.-H., et al. (2015). Improving performance and lifetime of small-molecule organic photovoltaic devices by using bathocuproine–fullerene cathodic layer. ACS Appl. Mater. Interfaces *7*, 9262–9273. https://doi.org/10.1021/acsami.5b01888.

18. Burlingame, Q., Song, B., Ciammaruchi, L., Zanotti, G., Hankett, J., Chen, Z., Katz, E.A., and Forrest, S.R. (2016). Reliability of small molecule organic photovoltaics with electron-filtering compound buffer layers. Adv. Energy Mater. *6*, 1601094. https://doi.org/10.1002/aenm.201601094.

19. Hermenau, M., Schubert, S., Klumbies, H., Fahlteich, J., Müller-Meskamp, L., Leo, K., and Riede, M. (2012). The effect of barrier performance on the lifetime of small-molecule organic solar cells. Sol. Energy Mater. Sol. Cells *97*, 102–108. https://doi.org/10.1016/j.solmat.2011.09.026.

20. Cai, Y., Li, Y., Wang, R., Wu, H., Chen, Z., Zhang, J., Ma, Z., Hao, X., Zhao, Y., Zhang, C., et al. (2021). A well-mixed phase formed by two compatible non-fullerene acceptors enables ternary organic solar cells with efficiency over 18.6%. Adv. Mater. *33*, e2101733. https://doi.org/10.1002/adma.202101733.

21. Li, C., Zhou, J., Song, J., Xu, J., Zhang, H., Zhang, X., Guo, J., Zhu, L., Wei, D., Han, G., et al. (2021). Non-fullerene acceptors with branched side chains and improved molecular packing to exceed 18% efficiency in organic solar cells. Nat. Energy *6*, 605–613. https://doi.org/10.1038/s41560-021-00820-x.

22. Liu, Q., Jiang, Y., Jin, K., Qin, J., Xu, J., Li, W., Xiong, J., Liu, J., Xiao, Z., Sun, K., et al. (2020). 18% Efficiency organic solar cells. Sci. Bull. (Beijing) *65*, 272–275. https://doi.org/10.1016/j.scib.2020.01.001.

23. Bao, S., Yang, H., Fan, H., Zhang, J., Wei, Z., Cui, C., and Li, Y. (2021). Volatilizable solid additive-assisted treatment enables organic solar cells with efficiency over 18.8% and fill factor exceeding 80%. Adv. Mater. *33*, e2105301. https://doi.org/10.1002/adma.202105301.

24. Han, Y., Dong, H., Pan, W., Liu, B., Chen, X., Huang, R., Li, Z., Li, F., Luo, Q., Zhang, J., et al. (2021). An efficiency of 16.46% and a T 80 lifetime of over 4000 h for the PM6:Y6 inverted organic solar cells enabled by surface acid treatment of the zinc oxide electron transporting layer. ACS Appl. Mater. Interfaces *13*, 17869–17881. https://doi.org/10.1021/acsami.1c02613.

25. Jiang, Y., Sun, L., Jiang, F., Xie, C., Hu, L., Dong, X., Qin, F., Liu, T., Hu, L., Jiang, X., et al. (2019). Photocatalytic effect of ZnO on the stability of nonfullerene acceptors and its mitigation by SnO 2 for nonfullerene organic solar cells. Mater. Horiz. *6*, 1438–1443. https://doi.org/10.1039/C9MH00379G.

26. Ahmad, J., Bazaka, K., Anderson, L.J., White, R.D., and Jacob, M.V. (2013). Materials and methods for encapsulation of OPV: a review. Renew. Sustain. Energy Rev. *27*, 104–117. https://doi.org/10.1016/j.rser.2013.06.027.

27. Tintori, F., Laventure, A., Koenig, J.D.B., and Welch, G.C. (2020). High open-circuit voltage roll-to-roll compatible processed organic photovoltaics. J. Mater. Chem. C *8*, 13430–13438. https://doi.org/10.1039/D0TC03614E.

28. Speller, E.M., Clarke, A.J., Aristidou, N., Wyatt, M.F., Francàs, L., Fish, G., Cha, H., Lee, H.K.H., Luke, J., Wadsworth, A., et al. (2019). Toward improved environmental stability of polymer:fullerene and polymer:nonfullerene organic solar cells: a common energetic origin of light- and oxygen-induced degradation. ACS Energy Lett. *4*, 846–852. https://doi.org/10.1021/acsenergylett.9b00109.

29. Lee, H.K.H., Telford, A.M., Röhr, J.A., Wyatt, M.F., Rice, B., Wu, J., de Castro Maciel, A., Tuladhar, S.M., Speller, E., McGettrick, J., et al. (2018). The role of fullerenes in the environmental stability of polymer:fullerene solar cells. Energy Environ. Sci. *11*, 417–428. https://doi.org/10.1039/C7EE02983G.

30. Hagler, T.W., Pakbaz, K., Voss, K.F., and Heeger, A.J. (1991). Enhanced order and electronic delocalization in conjugated polymers oriented by gel processing in polyethylene. Phys. Rev. B Condens. Matter *44*, 8652–8666. https://doi.org/10.1103/PhysRevB.44.8652.

31. Upama, M.B., Wright, M., Puthen-Veettil, B., Elumalai, N.K., Mahmud, M.A., Wang, D., Chan, K.H., Xu, C., Haque, F., and Uddin, A. (2016). Analysis of burn-in photo degradation in low bandgap polymer PTB7 using photothermal deflection spectroscopy. RSC Adv. *6*, 103899–103904. https://doi.org/10.1039/C6RA23288D.

32. Gotoh, T., Nonomura, S., Hirata, S., and Nitta, S. (1997). Photothermal bending spectroscopy and photothermal deflection spectroscopy of C60 thin films. Appl. Surf. Sci. *113–114*, 278–281. https://doi.org/10.1016/S0169-4332(96)00776-3.

33. Weu, A., Kress, J.A., Paulus, F., Becker-Koch, D., Lami, V., Bakulin, A.A., and Vaynzof, Y. (2019). Oxygen-induced doping as a degradation mechanism in highly efficient organic solar cells. ACS Appl. Energy Mater. *2*, 1943–1950. https://doi.org/10.1021/acsaem.8b02049.

34. Wang, K., Chen, H., Li, S., Zhang, J., Zou, Y., and Yang, Y. (2021). Interplay between intrachain and interchain excited states in donor–acceptor copolymers. J. Phys. Chem. B *125*, 7470–7476. https://doi.org/10.1021/acs.jpcb.1c03989.

35. Thomas, T.H., Harkin, D.J., Gillett, A.J., Lemaur, V., Nikolka, M., Sadhanala, A., Richter, J.M., Armitage, J., Chen, H., McCulloch, I., et al. (2019). Short contacts between chains enhancing luminescence quantum yields and carrier mobilities in conjugated copolymers. Nat. Commun. *10*, 2614. https://doi.org/10.1038/s41467-019-10277-y.

36. Thomas, T.H., Rivett, J.P.H., Gu, Q., Harkin, D.J., Richter, J.M., Sadhanala, A., Yong, C.K., Schott, S., Broch, K., Armitage, J., et al. (2019). Chain coupling and luminescence in high-mobility, low-disorder conjugated polymers. ACS Nano *13*, 13716–13727. https://doi.org/10.1021/acsnano.9b07147.

37. Yan, M., Rothberg, L.J., Papadimitrakopoulos, F., Galvin, M.E., and Miller, T.M. (1994). Spatially indirect excitons as primary photoexcitations in conjugated polymers. Phys. Rev. Lett. *72*, 1104–1107. https://doi.org/10.1103/PhysRevLett.72.1104.

38. Frankevich, E.L., Lymarev, A.A., Sokolik, I., Karasz, F.E., Blumstengel, S., Baughman, R.H., and Hörhold, H.H. (1992). Polaron-pair generation in poly(phenylene vinylenes). Phys. Rev. B Condens. Matter *46*, 9320–9324. https://doi.org/10.1103/PhysRevB.46.9320.

39. Menke, S.M., Cheminal, A., Conaghan, P., Ran, N.A., Greehnam, N.C., Bazan, G.C., Nguyen, T.-Q., Rao, A., and Friend, R.H. (2018). Order enables efficient electron-hole separation at an organic heterojunction with a small energy loss. Nat. Commun. *9*, 277. https://doi.org/10.1038/s41467-017-02457-5.

40. Razzell-Hollis, J., Wade, J., Tsoi, W.C., Soon, Y., Durrant, J., and Kim, J.-S. (2014). Photochemical stability of high efficiency

PTB7:PC $_{70}$ BM solar cell blends. J. Mater. Chem. A *2*, 20189–20195. https://doi.org/10.1039/C4TA05641H.

41. Wöpke, C., Göhler, C., Saladina, M., Du, X., Nian, L., Greve, C., Zhu, C., Yallum, K.M., Hofstetter, Y.J., Becker-Koch, D., et al. (2022). Traps and transport resistance are the next frontiers for stable non-fullerene acceptor solar cells. Nat. Commun. *13*, 3786. https://doi.org/10.1038/s41467-022-31326-z.

42. Nikolka, M., Nasrallah, I., Rose, B., Ravva, M.K., Broch, K., Sadhanala, A., Harkin, D., Charmet, J., Hurhangee, M., Brown, A., et al. (2017). High operational and environmental stability of high-mobility conjugated polymer field-effect transistors through the use of molecular additives. Nat. Mater. *16*, 356–362. https://doi.org/10.1038/nmat4785.

43. Zhang, Q., Chen, Y., Liu, X., and Fahlman, M. (2023). *In situ* near-ambient pressure X-ray photoelectron spectroscopy reveals the effects of water, oxygen and light on the stability of PM6:Y6 photoactive layers. J. Mater. Chem. C *11*, 3112–3118. https://doi.org/10.1039/D2TC04378E.

44. Brinkmann, K.O., Becker, T., Zimmermann, F., Kreusel, C., Gahlmann, T., Theisen, M., Haeger, T., Olthof, S., Tückmantel, C., Günster, M., et al. (2022). Perovskite–organic tandem solar cells with indium oxide interconnect. Nature *604*, 280–286. https://doi.org/10.1038/s41586-022-04455-0.

45. Gillett, A.J., Tonnelé, C., Londi, G., Ricci, G., Catherin, M., Unson, D.M.L., Casanova, D., Castet, F., Olivier, Y., Chen, W.M., et al. (2021). Spontaneous exciton dissociation enables spin state interconversion in delayed fluorescence organic semiconductors. Nat. Commun. *12*, 6640. https://doi.org/10.1038/s41467-021-26689-8.

46. Xiao, M., Carey, R.L., Chen, H., Jiao, X., Lemaur, V., Schott, S., Nikolka, M., Jellett, C., Sadhanala, A., Rogers, S., et al. (2021). Charge transport physics of a unique class of rigid-rod conjugated polymers with fused-ring conjugated units linked by double carbon-carbon bonds. Sci. Adv. *7*, 5280–5308. https://doi.org/10.1126/sciadv.abe5280.

47. de Mello, J.C., Wittmann, H.F., and Friend, R.H. (1997). An improved experimental determination of external photoluminescence quantum efficiency. Adv. Mater. *9*, 230–232. https://doi.org/10.1002/adma.19970090308.

48. Stoll, S., and Schweiger, A. (2006). EasySpin, a comprehensive software package for spectral simulation and analysis in EPR. J. Magn. Reson. *178*, 42–55. https://doi.org/10.1016/j.jmr.2005.08.013.

49. Cui, L., Butler, H.J., Martin-Hirsch, P.L., and Martin, F.L. (2016). Aluminium foil as a potential substrate for ATR-FTIR, transflection FTIR or Raman spectrochemical analysis of biological specimens. Anal. Methods *8*, 481–487. https://doi.org/10.1039/C5AY02638E.

50. Baikie, I.D., Grain, A.C., Sutherland, J., and Law, J. (2014). Dual mode Kelvin Probe: featuring ambient pressure photoemission spectroscopy and contact potential difference. Energy Procedia *60*, 48–56. https://doi.org/10.1016/j.egypro.2014.12.341.

51. Jiang, Z. (2015). *GIXSGUI*: a MATLAB toolbox for grazing-incidence X-ray scattering data visualization and reduction, and indexing of buried three-dimensional periodic nanostructured films. J. Appl. Crystallogr. *48*, 917–926. https://doi.org/10.1107/S1600576715004434.

52. Frisch, G.W., Schlegel, H.B., Scuseria, G.E., Robb, M.A., Cheeseman, J.R., Scalmani, G., Barone, V., Petersson, G.A., Nakatsuji, H., Li, X., et al. (2016). Gaussian 16, Rev. A.03 (Gaussian, Incorp.).

53. Tran, V.A., and Neese, F. (2020). Double-hybrid density functional theory for g-tensor calculations using gauge including atomic orbitals. J. Chem. Phys. *153*, 054105. https://doi.org/10.1063/5.0013799.

54. Neese, F., Wennmohs, F., Becker, U., and Riplinger, C. (2020). The ORCA quantum chemistry program package. J. Chem. Phys. *152*, 224108. https://doi.org/10.1063/5.0004608.

55. Thompson, A.P., Aktulga, H.M., Berger, R., Bolintineanu, D.S., Brown, W.M., Crozier, P.S., in 't Veld, P.J., Kohlmeyer, A., Moore, S.G., Nguyen, T.D., et al. (2022). LAMMPS – a flexible simulation tool for particle-based materials modeling at the atomic, meso, and continuum scales. Comput. Phys. Commun. *271*, 108171. https://doi.org/10.1016/j.cpc.2021.108171.

56. Mayo, S.L., Olafson, B.D., and Goddard, W.A. (1990). DREIDING: a generic force field for molecular simulations. J. Phys. Chem. *94*, 8897–8909. https://doi.org/10.1021/j100389a010.

57. Skånberg, R., Linares, M., König, C., Norman, P., Jönsson, D., Hotz, I., and Ynnerman, A. (2018). VIA-MD: visual interactive analysis of molecular dynamics. In MolVA '18: Proceedings of the Workshop on Molecular Graphics and Visual Analysis of Molecular Data, pp. 19–27.

58. Skanberg, R., Falk, M., Linares, M., Ynnerman, A., and Hotz, I. (2022). Tracking internal frames of reference for consistent molecular distribution functions. IEEE Trans. Vis. Comput. Graph. *28*, 3126–3137. https://doi.org/10.1109/TVCG.2021.3051632.

59. Skånberg, R., Linares, M., König, C., Norman, P., Jönsson, D., Hotz, I., and Ynnerman, A. (2018). VIA-MD: Visual Interactive Analysis of Molecular Dynamics. InMolVa@ EuroVis, 19. https://doi.org/10.2312/molva.20181102.

60. Lu, T., and Chen, F. (2012). Multiwfn: a multifunctional wavefunction analyzer. J. Comput. Chem. *33*, 580–592. https://doi.org/10.1002/jcc.22885.

61. Masood, T.B., Thygesen, S.S., Linares, M., Abrikosov, A.I., Natarajan, V., and Hotz, I. (2021). Visual analysis of electronic densities and transitions in molecules. Comput. Graphics Forum *40*, 287–298. https://doi.org/10.1111/cgf.14307.